Cite as: L. Liu *et al.*, *Science*
10.1126/science.aba9413 (2020).

Making ultrastrong steel tough by grain-boundary delamination

L. Liu[1]*, Qin Yu[2]*, Z. Wang[1], Jon Ell[2,3], M. X. Huang[1]†, Robert O. Ritchie[2,3]†

[1]Department of Mechanical Engineering, The University of Hong Kong, Pokfulam Road, Hong Kong, China. [2]Materials Sciences Division, Lawrence Berkeley National Laboratory, Berkeley, CA 94720, USA. [3]Department of Materials Science and Engineering, University of California, Berkeley, CA 94720, USA.

***These authors contributed equally to this work.**

†Corresponding author. Email: mxhuang@hku.hk (M.X.H.); roritchie@lbl.gov (R.O.R.)

Developing ultrahigh strength steels that are ductile, fracture resistant, and cost-effective would be attractive for a variety of structural applications. We show that improved fracture resistance in a steel with an ultrahigh yield strength of nearly 2GPa can be achieved by activating delamination toughening coupled with transformation induced plasticity. Delamination toughening associated with intensive but controlled cracking at Mn-enriched prior-austenite grain boundaries normal to the primary fracture surface dramatically improves the overall fracture resistance. As a result, fracture under plane-strain conditions is automatically transformed into a series of fracture processes in "parallel" plane-stress conditions through the thickness. The present "high-strength induced multi-delamination" strategy offers a different pathway to develop engineering materials with ultra-high strength and superior toughness at economical materials cost.

Lightweight yet cost-efficient structural materials with superior mechanical properties are continually sought after in engineering applications to meet the demands of sustainable economy development. Unfortunately, attaining high strength is usually at the expense of deteriorating toughness, which invariably is a major concern for safety-critical applications (*1*, *2*). The strengthening mechanisms in structural metals and alloys are built on the fundamental principle of inhibiting, or blocking, dislocation slip by introducing various obstacles at different length-scales (*3*, *4*). However, abundant dislocations entangled in small imperfections can give rise to the localized stress concentrations that can cause crack initiation which eventually can lead to catastropic failure (*1*, *5*). A mainstream effort to overcome the strength-toughness trade-off is focused on tailoring the microstructure or designing materials by solid-solution alloying. Multi-element high and medium-entropy alloys possess exceptional damage tolerance at cryogenic temperatures because of a deformation-induced nano-twinning mechanism (*6*, *7*). Maraging steels are another example as they are recognized as the strongest metal alloys with acceptable damage tolerance for aerospace applications. However, maraging steels contain a large amount of costly alloying elements like nickel (17-19 wt %), cobalt (8-12 wt %) and molybdenum (3-5 wt %) (*8*). Although the maraging steel alloying strategy is a perfect vehicle to attain superior mechanical performance, economical mass production and recycling are not feasible due to costs and environmental concerns (*3*, *9*). Reducing the average grain size is a different non-alloying pathway to enhance the strength-toughness combination. However, this approach can be limiting because the strengthening is usually achieved at the sacrifice of losing ductility (*10*, *11*). We show here that exceptional damage-tolerance can be achieved in an ultrastrong steel, with a simple composition and cost-effective processing route for fabrication. We demonstrate that increasing the yield strength is not detrimental to the toughness, but instead it can facilitate the activation of a delamination toughening (*12*, *13*) mechanism. This substantially enhances the toughness. Specifically, the ultrahigh yield strength enables a secondary fracture mode, delamination cracking, at interfaces normal to the primary fracture surface. Multiple separated laminated ligaments develop near the fracture surface because of the delamination events, providing an extra energy release rate for fracture as well as enhancing crack-tip blunting, collectively elevating the overall fracture toughness. Such delamination toughening combined with transformation-induced plasticity (TRIP) toughening are rarely realized simutaneously in structural materals. The combination enables an intringuing combination of strengh, ductility and toughness properties in our steel.

Our steel has a chemical composition of Fe-9.95%Mn-0.44%C-1.87%Al-0.67%V (weight percent) and was fabricated by a deformed and partitioned treatment (fig. S1) (*14*). Starting with an almost fully austenitic microstructure (fig. S2), the prior-austenite grains are extensively elongated along the rolling direction (RD) during the initial hot rolling and warm rolling processes (*14*, *15*). The austenite partially transforms to martensite during the subsequent cold rolling, resulting in a lamellar martensite/austenite duplex microstructure (Fig. 1A), which contains a volume fraction of austenite, measured at 47.5% by neutron diffraction (fig. S3). Partitioning is finally performed to optmize the mechanical stability of retained austenite by C partitioning from martensite to austenite (fig. S4) (*14*). The martensitic matrix (α') is composed of nano-sized grains decorated by intensive dislocations (fig. S5). The dislocation density of martensite matrix was determined by neutron diffraction to be 2.43×10^{16} m^{-2} which is at least one order higher than that of other martensitic steels (fig. S6); further details of this calculation based on neutron diffraction measurements are given in ref. (*16*). The austenite (γ) phase displays a stretched lamellar-shaped grain structure with dimensions of hundreds of micrometers along the RD, dozens of micrometers in the transverse direcrtion (TD), and a few micrometers in the normal direction (ND) (Fig. 1A). Of particular note is that the prior-austenite grain boundaries (PAGBs) are retained during cold rolling where some austenite grains transform to martensite; this is indicated by the black dotted lines in the three-dimensional (3D) stereographic microstructure in Fig. 1B, reconstructed from the PAGBs maps. Further atomic-scale composition analysis of the present steel by 3D atom probe topography (APT) shows segregation of Mn and C to the PAGB [Fig. 1C, detailed explanation in (*16*)]. No segregation of P, S and other harmful elements to the PAGB was detected. To better illustrate the laminated duplex microstructure, we constructed a schematic 3D model (Fig. 1D).

To evaluate the mechanical properties of the ultrastrong steel, we characterized the tensile properties and the *J*-integral based crack-resistance (J-Δa) R-curves in both the RD and TD orientations in ambient air. The RD (or TD) dog-bone shaped tensile specimen was strained along (or perpendicular to) the elongated austenitic grains (Fig. 2A). Correspondingly, the notch and crack propagation direction in the RD (or TD) compact-tension C(T) fracture toughness specimen were aligned perpendicular to (or parallel to) the elongated austenitic grains. Benefiting from the unusually high dislocation density, tensile loading along the RD yields a superior combination of strength and ductility (Fig. 2B) (*14*). Specifically, the upper yield strength (σ_{yu}), the ultimate tensile strength (σ_{uts}) and the uniform elongation (ε_u) were determined to be 1,978 MPa, 2,144 MPa and 19.0%, respectively (Fig. 2B and table S1). Properties in the loading direction along the TD are also sound with a very high ultimate tensile strength of 2,048 MPa similar to that for the RD orientation, but plastic deformation begins to proceed earlier; the 0.2%-offset yield strength (σ_y) in the TD orientation was measured to be 1,714 MPa.

In view of its ultrahigh strength and plastic deformation capacity, we evaluated the fracture resistance of the present steel by measuring *J*-integral based R-curves, i.e., J as a function of the stable crack extension, Δa, using the C(T) specimens in accordance with the ASTM Standard E1820 (*17*). Our steel displays a modest fracture toughness when loaded along TD, presenting an average J_{Ic}, of 19.6 kJ·m^{-2} at crack initiation (Fig. 2C and table S1). The crack-resistance (R-curve) behavior in the TD slightly rises as the crack extends, resulting in a valid crack-growth toughness of J_{ss} = 28.7 kJ·m^{-2} at a crack extension Δa of ~1 mm. These fracture properties are comparable to those of the best strong-yet-tough materials, such as 18Ni 300-grade maraging steels (*18*, *19*) and commercial-aircraft-quality 300M and 4340 steels (*20*, *21*). In spite of a higher yield strength of the RD tensile specimens, the R-curve in the RD orientation reveals an even better crack resistance, showing a crack-initiation toughness J_{Ic} of 46.9 kJ·m^{-2} and a crack-growth toughness J_{ss} of 84.6 kJ·m^{-2} as the crack extends to Δa ~ 1 mm (Fig. 2C and table S1). These toughness values in the RD are almost 1.5 and 2 times higher than those in the TD, respectively. According to the standard mode-I *J*-*K* equivalence relationship, the crack-initiation toughness, K_{JIc} of the RD and TD specimens were determined to be 101.5 and 65.4 MPa·m$^{1/2}$, respectively. Likewise, the crack-growth toughness at Δa ~1 mm, K_{ss}, was 136.4 and 79.4 MPa·m$^{1/2}$ for the RD and TD specimens, respectively. These are very high values of the crack-initiation and crack-growth toughnesses in our ultrastrong steel that are not found in any other existing structural materials at a comparable yield strength (~2 GPa).

To illuminate the underlying toughening mechanisms responsible for the exceptional damage tolerance of the ultrastrong steel, we characterized the microstructures on various sections of the RD and TD C(T) specimens (Fig. 3, A and E). Featured regions on the fracture surfaces characterized by scanning electron microscopy (SEM) show the existence of multiple thin-layer delamination bands in both RD and TD orientations (Fig. 3, B and F). Observed from the fracture surface, the original ~1.4 mm-thick RD specimens were delaminated through the thickness into several thin layers with their inter-spacings (or delamination cracks) "penetrating" into the material along the planes perpendicular to the fracture surface. Moreover, delamination cracks at different length-scales were developed in the present steel, resulting in numerous delamination bands sized in the range of several micrometers (Region A in Fig. 3B). The thickness of these delamination ligaments was remarkable thinner than that in other structural materials containing delimination cracks (*12*, *13*). Delamination was also present in the TD specimens, but the delamination cracks were fewer in number and shorter in length than those in the RD specimens. The microstructure in the vicinity of the delamination cracks in the through-thickness sections normal to the fracture surface was further characterized to clarify the micro-mechanisms associated with the delamination cracks (Fig. 3, C and G). Based on the statistical distribution of the crack lengths (shown in figs. S7 and S8), the delamination cracks in the RD specimens can be categrizied into two groups: short cracks with lengths < ~50 μm (blue arrows in Fig. 3C) and longer cracks with lengths > ~50 μm (dark red arrows in Fig. 3C). Moreover, slender cracks disconnected from the fracture surface (pink arrows in Fig. 3C) were usually observed in the vicinity of the long delamination cracks. Further characterization at the tips of the delamination cracks clearly indicated that these cracks propagate predominantly along the PAGBs (Fig. 3C). In the case of the TD specimens, only short delamination cracks with lengths shorter than 50 μm were observed (Fig. 3G). Clearly, loading along the RD results in a much larger tendency for delamination.

The activation of delamination toughening requires two necessary conditions: intrinsically and microstructrally, the existence of "relatively weak interfaces", where delamination takes place; mechanically, with a "high mechanical stress" that exceeds the critical fracture stress of the "relatively weak interfaces". From our characterization of the locations at delamination crack tips, the Mn-enriched PAGBs in our steel serve as the "relatively weak interfaces" and preferential sites for the initiation and propagation of the delamination microcracks (Fig. 3, C and G). Actually, the Mn-enriched PAGBs still have a high level of cohesion strength, but they are just not as strong as the grain interior due to the segregation of Mn (Fig. 1C) (*22*, *23*). By comparison, such delaminations do not occur in maraging steels, no matter how high their yield strengths are, as there are no such interfaces and preferential sites along the boundaries with reduced cohesion.

From the perspective of the mechanical driving force, a triaxial tensile stress-state exists ahead of a crack tip under plane-strain conditions. The material in front of the crack tip is subjected to a tensile stress (σ_2 in fig. S9A) along the thickness direction (ND in Fig. 1A). When the tensile stress σ_2 that is perpendicular to the PAGBs is sufficiently high to reach the critical fracture stress of the Mn-enriched PAGBs (Fig. 3A), delamination will occur. To meet this requirement, the material should have sufficiently high yield strength so that a high external applied stress is required. A higher external applied stress will lead to a higher σ_2 at the crack tip. For certain structural materials containing weak interfaces, delamination cracks are mainly formed at low temperatures where the interfaces may be more brittle and the through-thickness stresses are larger. This leads to the fascinating effect that such alloys, e.g., certain Al-Li alloys (*12*) and ultrafine-grained low alloy steels (*24*, *25*), become tougher at cryogenic temperatures compared to ambient temperature. As demonstrated here, the present steel possesses ultrahigh yield strength due to its high dislocation density, and Mn-enriched PAGBs with relatively low cohesion as compared to the grain interior, acting as the preferential delamination sites; this meets the two necessary requirments to activate delamianation toughening and leads to its exceptional room-temperature fracture toughness for a metallic alloy with a yield strength in the 2 GPa range.

As a consequence of the multiple delamination cracks occurring ahead of the crack front and perpendicular to the crack plane, the expected fracture under plane-strain conditions is transformed into a series of fracture processes in "parallel" plane-stress ligaments through the thickness which individually display a far higher (plane-stress) toughness than for a single (full-thickness) plane-strain section (fig. S9B). In parallel, numerous new interfaces generated during the delamination process consume energy, which effectively increases the energy release rate to contribute to the exceptional fracture toughness. Our current study further reveals that the delamination toughening is affected by the relative orientations of the delamination crack path with respect to the elongated duplex structure. The length of the PAGBs along RD are almost three times of that parallel to TD due to the large rolling reduction (Fig. 1B). As the delamination cracks propagate along the elongated PAGBs parallel to RD in the RD specimens, longer delamination cracks are developed (Fig. 3C). However, delamination cracks extend with short PAGBs parallel to the TD on the through-thickness section in the TD specimen. Furthermore, numerous PAGBs, aligned perpendicular to the crack path, are developed in the TD specimen. These grain boundaries are effective obstacles to retard the propagation of delamination cracks (Fig. 3G). Therefore, the longer (or shorter) delamination cracks developed in the RD (or TD) specimens give rise to a larger (or smaller) toughening effect, which is consistent with the higher (or lower) values of the measured toughness in these orientations.

The present steel also displays a TRIP effect during crack advance. The TRIP-toughening is due to an in situ austenite to martensite transformation that is triggered in the vicinity of the crack tip, where an initial duplex martensitic/austenitic microstructure (Fig. 1A) is transformed to an almost fully martensitic microstructure (Fig. 3, D and H) after crack propagation. Due to the lattice-parameter difference between martensite and parent austenite, a compressive residual stress is likely introduced by the TRIP effect in the vicinity of crack tip to further resist crack propagation (*26*). In addition, TRIP effect can serve to promote strain hardening which, in turn, enhances the uniform ductility by delaying the onset of the necking instability to provide additional intrinsic toughening to resist crack propagation (*27*, *28*).

Similar to the delamination toughening, the TRIP-toughening is also a function of the crack extension orientations. A larger-sized TRIP zone is realized in the RD specimen (Fig. 3D) where the main crack propagates perpendicular to the elongated austenite. In contrast, a small-sized TRIP-zone is produced (Fig. 3H) in the TD specimen because the growth of the TRIP-zone is significantly restricted by the PAGBs parallel to the elongated austenite lamellae (*28*). This is illustrated in the schematic figures in Fig. 3, D and H. Consistently, higher (or lower) toughness values exhibited in the RD (or TD) specimens are ascribed to the stronger (or weaker) TRIP toughening effect induced by the larger (or smaller)-sized TRIP zone.

To demonstrate how the excellent damage-tolerance in our steel compares to other ultrahigh strength structural materials, we show in Fig. 4 an Ashby map of the crack-initiation fracture toughness versus yield strength. Our steel exhibits a comparable yield strength to some of the strongest existing metallic materials, namely maraging steels, but with an initiation toughness (K_c) that is almost a factor of two higher. Indeed, our steel displays a toughness comparable to titanium alloys but with a factor of two higher strength. The exceptional combination of strength and toughness clearly demonstrates that the "high-strength induced multi-delamination" mechanism can be highly effective in maximizing the mechanical properties of high-strength structural materials while minimizing material cost. Our material design principle that exploits high strength combined with relatively weak interfaces, is one that we believe can be widely applied to optimize the mechanical performance of materials with ultrahigh strength.

REFERENCES AND NOTES

1. R. O. Ritchie, The conflicts between strength and toughness. *Nat. Mater.* **10**, 817–822 (2011). doi:10.1038/nmat3115 Medline
2. K. Lu, The future of metals. *Science* **328**, 319–320 (2010). doi:10.1126/science.1185866 Medline
3. X. Li, K. Lu, Playing with defects in metals. *Nat. Mater.* **16**, 700–701 (2017). doi:10.1038/nmat4929 Medline
4. K. Lu, L. Lu, S. Suresh, Strengthening materials by engineering coherent internal boundaries at the nanoscale. *Science* **324**, 349–352 (2009). doi:10.1126/science.1159610 Medline
5. M. JW, Z. Guo, K. CR, Y.-H. Kim, The limits of strength and toughness in steel. *ISIJ Int.* **41**, 599–611 (2001).
6. B. Gludovatz, A. Hohenwarter, D. Catoor, E. H. Chang, E. P. George, R. O. Ritchie, A fracture-resistant high-entropy alloy for cryogenic applications. *Science* **345**, 1153–1158 (2014). doi:10.1126/science.1254581 Medline
7. B. Gludovatz, A. Hohenwarter, K. V. S. Thurston, H. Bei, Z. Wu, E. P. George, R. O. Ritchie, Exceptional damage-tolerance of a medium-entropy alloy CrCoNi at cryogenic temperatures. *Nat. Commun.* **7**, 10602 (2016). doi:10.1038/ncomms10602 Medline
8. S. Floreen, The physical metallurgy of maraging steels. *Metallurg. Rev.* **13**, 115–128 (1968).
9. X. Li, K. Lu, Improving sustainability with simpler alloys. *Science* **364**, 733–734 (2019). doi:10.1126/science.aaw9905 Medline
10. K. Lu, Nanomaterials. Making strong nanomaterials ductile with gradients. *Science* **345**, 1455–1456 (2014). doi:10.1126/science.1255940 Medline
11. Y. Wang, M. Chen, F. Zhou, E. Ma, High tensile ductility in a nanostructured metal. *Nature* **419**, 912–915 (2002). doi:10.1038/nature01133 Medline
12. K. T. Venkateswara Rao, W. Yu, R. O. Ritchie, Cryogenic toughness of commercial aluminum-lithium alloys: Role of delamination toughening. *Metall. Trans., A, Phys. Metall. Mater. Sci.* **20**, 485–497 (1989). doi:10.1007/BF02653929
13. K. S. Chan, Evidence of a thin sheet toughening mechanism in Al– Fe– X alloys. *Metall. Trans., A, Phys. Metall. Mater. Sci.* **20**, 155–164 (1989). doi:10.1007/BF02647502
14. B. B. He, B. Hu, H. W. Yen, G. J. Cheng, Z. K. Wang, H. W. Luo, M. X. Huang, High dislocation density-induced large ductility in deformed and partitioned steels. *Science* **357**, 1029–1032 (2017). doi:10.1126/science.aan0177 Medline
15. L. Liu, B. B. He, M. X. Huang, Processing–Microstructure Relation of Deformed and Partitioned (D&P) Steels. *Metals (Basel)* **9**, 695 (2019). doi:10.3390/met9060695
16. Materials and methods are available as Supplementary Materials on Science online.
17. ASTM International, *E1820-17a Standard Test Method for Measurement of Fracture Toughness* (ASTM International, 2017).
18. C. Carter, Stress corrosion crack branching in high-strength steels. *Eng. Fract. Mech.* **3**, 1–13 (1971). doi:10.1016/0013-7944(71)90047-6
19. Y. He, K. Yang, W. Qu, F. Kong, G. Su, Strengthening and toughening of a 2800-MPa grade maraging steel. *Mater. Lett.* **56**, 763–769 (2002). doi:10.1016/S0167-577X(02)00610-9
20. R. O. Ritchie, Influence of microstructure on near-threshold fatigue-crack propagation in ultra-high strength steel. *Met. Sci.* **11**, 368–381 (1977). doi:10.1179/msc.1977.11.8-9.368
21. R. O. Ritchie, B. Francis, W. L. Server, Evaluation of toughness in AISI 4340 alloy steel austenitized at low and high temperatures. *Metall. Trans., A, Phys. Metall. Mater. Sci.* **7**, 831–838 (1976). doi:10.1007/BF02644080
22. M. Kuzmina, D. Ponge, D. Raabe, Grain boundary segregation engineering and austenite reversion turn embrittlement into toughness: Example of a 9 wt.% medium Mn steel. *Acta Mater.* **86**, 182–192 (2015). doi:10.1016/j.actamat.2014.12.021
23. N. Heo, J. Nam, Y.-U. Heo, S.-J. Kim, Grain boundary embrittlement by Mn and eutectoid reaction in binary Fe–12Mn steel. *Acta Mater.* **61**, 4022–4034 (2013). doi:10.1016/j.actamat.2013.03.016
24. Y. Kimura, T. Inoue, F. Yin, K. Tsuzaki, Inverse temperature dependence of toughness in an ultrafine grain-structure steel. *Science* **320**, 1057–1060 (2008). doi:10.1126/science.1156084 Medline
25. J. W. Morris Jr., Stronger, tougher steels. *Science* **320**, 1022–1023 (2008). doi:10.1126/science.1158994 Medline
26. W. Bleck, X. Guo, Y. Ma, The TRIP effect and its application in cold formable sheet steels. *Steel Res. Int.* **88**, 1700218 (2017). doi:10.1002/srin.201700218
27. R. H. Leal, Transformation toughening of metastable austenitic steels. Ph.D. Thesis, Massachusetts Institute of Technology, (1984).
28. M. M. Wang, C. C. Tasan, D. Ponge, A. C. Dippel, D. Raabe, Nanolaminate transformation-induced plasticity–twinning-induced plasticity steel with dynamic strain partitioning and enhanced damage resistance. *Acta Mater.* **85**, 216–228 (2015). doi:10.1016/j.actamat.2014.11.010
29. M. Linaza, J. Romero, J. Rodriguez-Ibabe, J. Urcola, Improvement of fracture toughness of forging steels microalloyed with titanium by accelerated cooling after hot working. *Scr. Metall. Mater.* **29**, 1217–1222 (1993). doi:10.1016/0956-716X(93)90112-6
30. M. E. Haque, K. Sudhakar, ANN back-propagation prediction model for fracture toughness in microalloy steel. *Int. J. Fatigue* **24**, 1003–1010 (2002). doi:10.1016/S0142-1123(01)00207-9
31. S. K. Putatunda, Fracture toughness of a high carbon and high silicon steel. *Mater. Sci. Eng. A* **297**, 31–43 (2001). doi:10.1016/S0921-5093(00)01272-7
32. J. Kobayashi, D. Ina, A. Futamura, K.-i. Sugimoto, Fracture toughness of an advanced ultrahigh-strength TRIP-aided steel. *ISIJ Int.* **54**, 955–962 (2014). doi:10.2355/isijinternational.54.955
33. A. Bayram, A. Uğuz, M. Ula, Effects of microstructure and notches on the mechanical properties of dual-phase steels. *Mater. Charact.* **43**, 259–269 (1999). doi:10.1016/S1044-5803(99)00044-3
34. L. Xiong, Z. You, S. Qu, L. Lu, Fracture behavior of heterogeneous nanostructured 316L austenitic stainless steel with nanotwin bundles. *Acta Mater.* **150**, 130–138 (2018). doi:10.1016/j.actamat.2018.02.065

35. J. E. Pawel, D. J. Alexander, M. L. Grossbeck, A. W. Longest, A. F. Rowcliffe, G. E. Lucas, S. Jitsukawa, A. Hishinuma, K. Shiba, Fracture toughness of candidate materials for ITER first wall, blanket, and shield structures. *J. Nucl. Mater.* **212-215**, 442–447 (1994). doi:10.1016/0022-3115(94)90101-5
36. L. Van Swam, R. Pelloux, N. Grant, Properties of maraging steel 300 produced by powder metallurgy. *Powder Metall.* **17**, 33–45 (1974). doi:10.1179/pom.1974.17.33.004
37. R. O. Ritchie, Near-threshold fatigue crack propagation in ultra-high strength steel: Influence of load ratio and cyclic strength. *J. Eng. Mater. Technol.* **99**, 195–204 (1977). doi:10.1115/1.3443519
38. G. Lai, W. Wood, R. Clark, V. Zackay, E. R. Parker, The effect of austenitizing temperature on the microstructure and mechanical properties of as-quenched 4340 steel. *Metall. Trans.* **5**, 1663–1670 (1974). doi:10.1007/BF02646340
39. H. Aglan, Z. Liu, M. Hassan, M. Fateh, Mechanical and fracture behavior of bainitic rail steel. *J. Mater. Process. Technol.* **151**, 268–274 (2004). doi:10.1016/j.jmatprotec.2004.04.073
40. C. Garcia-Mateo, F. Caballero, Ultra-high-strength bainitic steels. *ISIJ Int.* **45**, 1736–1740 (2005). doi:10.2355/isijinternational.45.1736
41. M. D. Demetriou, M. E. Launey, G. Garrett, J. P. Schramm, D. C. Hofmann, W. L. Johnson, R. O. Ritchie, A damage-tolerant glass. *Nat. Mater.* **10**, 123–128 (2011). doi:10.1038/nmat2930 Medline
42. N. Kamp, I. Sinclair, M. Starink, Toughness-strength relations in the overaged 7449 Al-based alloy. *Metall. Mater. Trans., A Phys. Metall. Mater. Sci.* **33**, 1125–1136 (2002). doi:10.1007/s11661-002-0214-2
43. M. Niinomi, Mechanical properties of biomedical titanium alloys. *Mater. Sci. Eng. A* **243**, 231–236 (1998). doi:10.1016/S0921-5093(97)00806-X
44. R. Mirshams, C. Xiao, S. Whang, W. Yin, R-curve characterization of the fracture toughness of nanocrystalline nickel thin sheets. *Mater. Sci. Eng. A* **315**, 21–27 (2001). doi:10.1016/S0921-5093(01)01213-8
45. A. Singh, L. Tang, M. Dao, L. Lu, S. Suresh, Fracture toughness and fatigue crack growth characteristics of nanotwinned copper. *Acta Mater.* **59**, 2437–2446 (2011). doi:10.1016/j.actamat.2010.12.043
46. L. Liu, B. B. He, M. X. Huang, Engineering heterogeneous multiphase microstructure by austenite reverted transformation coupled with ferrite transformation. *JOM* **71**, 1322–1328 (2019). doi:10.1007/s11837-019-03365-3
47. H. Bhadeshia, R. Honeycombe, *Steels: Microstructure and Properties*. Butterworth-Heinemann, 2017.
48. P. J. Withers, Depth capabilities of neutron and synchrotron diffraction strain measurement instruments. I. The maximum feasible path length. *J. Appl. Cryst.* **37**, 596–606 (2004). doi:10.1107/S0021889804012737
49. B. H. Toby, R. B. Von Dreele, GSAS-II: The genesis of a modern open-source all purpose crystallography software package. *J. Appl. Cryst.* **46**, 544–549 (2013). doi:10.1107/S0021889813003531
50. M. Wang, M. Huang, Abnormal TRIP effect on the work hardening behavior of a quenching and partitioning steel at high strain rate. *Acta Mater.* **188**, 551–559 (2020). doi:10.1016/j.actamat.2020.02.035
51. T. Ungár, J. Gubicza, G. Ribárik, A. Borbély, Crystallite size distribution and dislocation structure determined by diffraction profile analysis: Principles and practical application to cubic and hexagonal crystals. *J. Appl. Cryst.* **34**, 298–310 (2001). doi:10.1107/S0021889801003715
52. T. Ungár, I. Dragomir, Á. Révész, A. Borbély, The contrast factors of dislocations in cubic crystals: The dislocation model of strain anisotropy in practice. *J. Appl. Cryst.* **32**, 992–1002 (1999). doi:10.1107/S0021889899009334
53. T. Ungár, I. Groma, M. Wilkens, Asymmetric X-ray line broadening of plastically deformed crystals. II. Evaluation procedure and application to [001]-Cu crystals. *J. Appl. Cryst.* **22**, 26–34 (1989). doi:10.1107/S0021889888009720
54. A. Devaraj, D. E. Perea, J. Liu, L. M. Gordon, T. J. Prosa, P. Parikh, D. R. Diercks, S. Meher, R. P. Kolli, Y. S. Meng, S. Thevuthasan, Three-dimensional nanoscale characterisation of materials by atom probe tomography. *Int. Mater. Rev.* **63**, 68–101 (2018). doi:10.1080/09506608.2016.1270728

ACKNOWLEDGMENTS

L.H. He and J. Chen are acknowledged for their help on the neutron powder diffraction experiments which were performed at GPPD of the China Spallation Neutron Source (CSNS), Dongguan, China. J.H. Luan and Z.B. Jiao are acknowledged for their help on the APT experiments conducted at the Inter-University 3D Atom Probe Tomography Unit of City University of Hong Kong. We thank B.B. He for his assistance with the preparation of the material, and M. Wang for help with the determination of the dislocation density. Finally, we thank Prof. K. Lu for his insightful comments on the paper. **Funding:** M.X.H. acknowledges the financial support from the National Key Research and Development Program of China (No. 2019YFA0209900, 2017YFB0304401), National Natural Science Foundation of China (No. U1764252) and Research Grants Council of Hong Kong (No. R7066-18, 17255016, 17210418). Q.Y. and R.O.R. acknowledge financial support to the Mechanical Behavior of Materials Program (KC13) at the Lawrence Berkeley National Laboratory (LBNL) provided by the U.S. Department of Energy, Office of Science, Basic Energy Sciences, Materials Sciences and Engineering Division under contract no. DE-AC02-05-CH11231. EBSD experiments were carried out at LBNL's Molecular Foundry supported by the Office of Science, Office of Basic Energy Sciences, of the U.S. Department of Energy under the same contract number. **Author contributions:** M.X.H., Q.Y., and R.O.R designed the research. M.X.H. and R.O.R. supervised the study. L.L. fabricated the steel material. Q.Y., J.E. and L.L. performed the mechanical characterization. L.L., Q.Y. and Z.W. conducted the SEM and EBSD characterizations. L.L. worked on the TEM characterization. L.L. and Z.W conducted the APT measurement and the neutron diffraction characterization. L.L., Q.Y., M.X.H. and R.O.R. analyzed the data and wrote the manuscript. All the authors discussed the results and commented on the manuscript. **Competing interests:** The authors declare no competing interests. **Data and materials availability:** Data are available in the manuscript and supplementary materials.

SUPPLEMENTARY MATERIALS

science.sciencemag.org/cgi/content/full/science.aba9413/DC1
Materials and Methods
Supplementary Text
Figs. S1 to S9
Tables S1 and S2
References (*46*–*54*)

17 January 2020; accepted 27 April 2020
Published online 7 May 2020
10.1126/science.aba9413

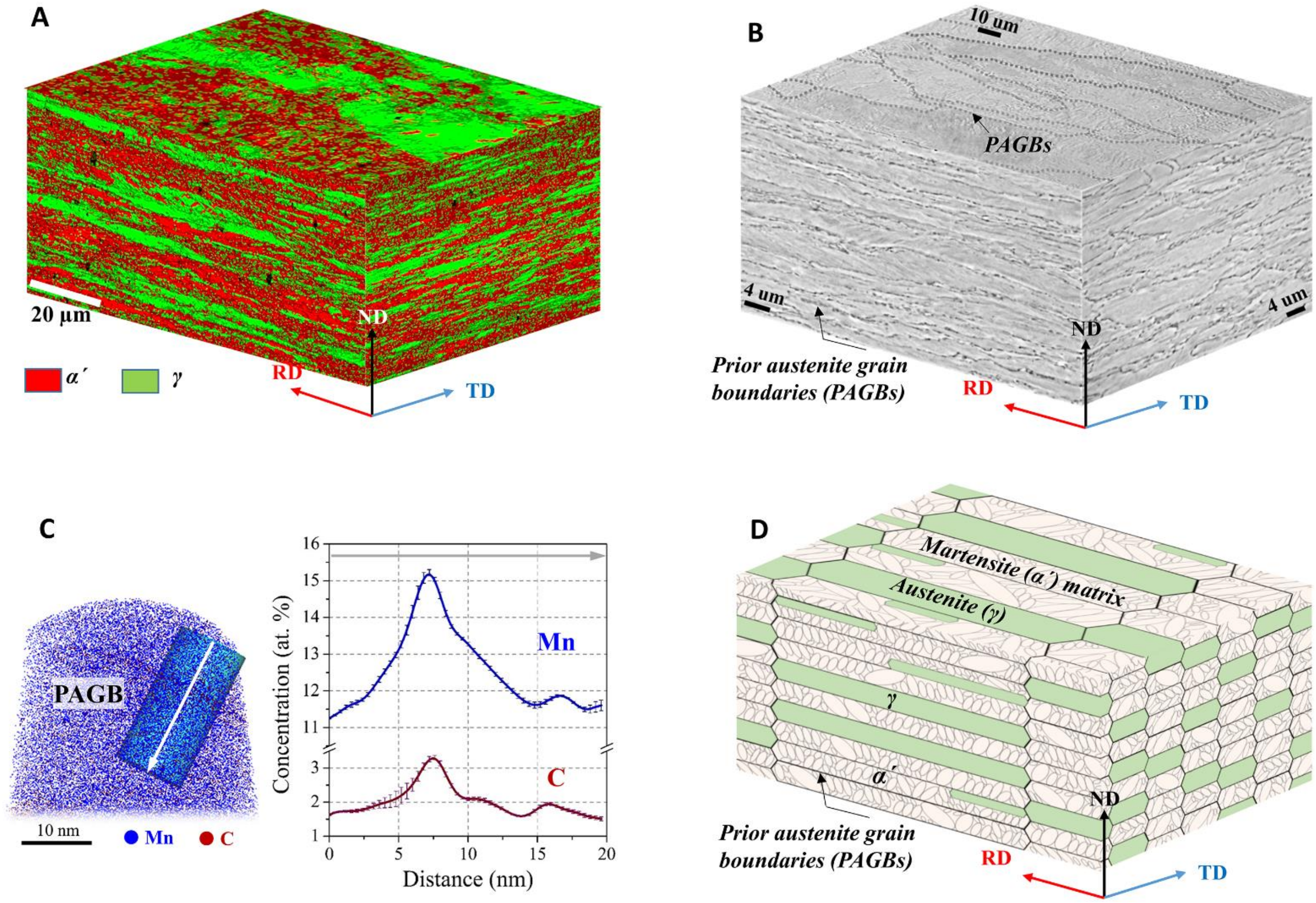

Fig. 1. Microstructure of the present steel. (**A**) 3D stereographic microstructure reconstructed by EBSD phase maps scanned on the orthotropic planes perpendicular to the rolling direction (RD), transverse direction (TD), and normal direction (ND), respectively. A heterogeneous laminated duplex microstructure comprising martensitic matrix (α′) and elongated austenite (γ) lamellae is exhibited in the present steel. Retained austenite grains are elongated along the RD and slightly stretched along the TD. (**B**) 3D stereographic microstructure reconstructed by the prior-austenite grain boundaries (PAGBs) maps imaged by SEM. The PAGBs are marked by the black dotted lines and show a heterogeneous distribution. (**C**) 3D ion concentration map, which contains a PAGB and a corresponding 1-D concentration profile across the boundary, shows the segregation of Mn and C to the PAGB. (**D**) Schematic 3D model illustrates the microstructural features of the heterogeneous microstructure of the present steel.

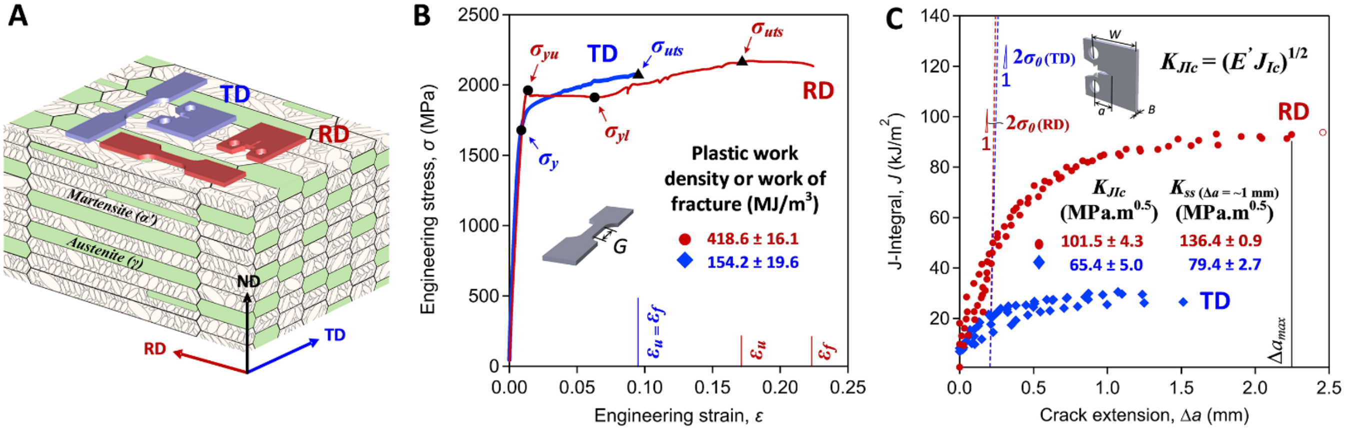

Fig. 2. **Tensile and fracture properties of the present steel.** (**A**) Schematic diagram describing the orientations of the dog-bone shaped tensile specimens and the compact-tension C(T) specimens relative to the thin-sheet steel. (**B**) Engineering stress-strain curves of the present steel deformed under tension along the RD and TD orientations. (**C**) The *J*-integral based resistance curves (*J*-R curves) measured from the C(T) specimens at room temperature.

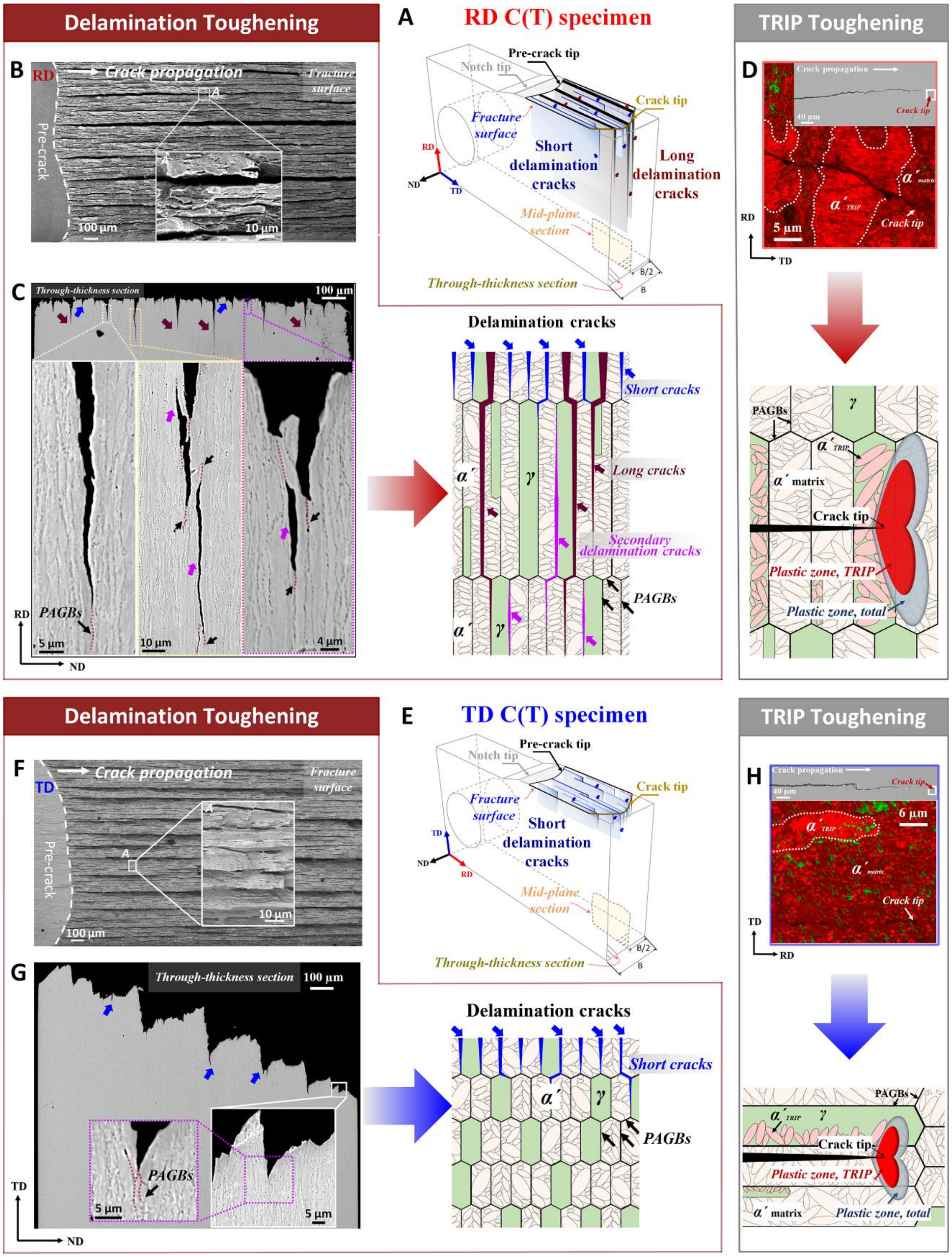

Delamination Toughening
A
RD C(T) specimen
TRIP Toughening
B
Crack propagation
Fracture surface
Pre-crack
Pre-crack tip
Notch tip
Crack tip
Fracture surface
Short delamination cracks
Long delamination cracks
Mid-plane section
Through-thickness section
D
Crack propagation
Crack tip
5 µm
Crack tip
C
Through-thickness section
Delamination cracks
Short cracks
Long cracks
Secondary delamination cracks
PAGBs
Crack tip
Plastic zone, TRIP
Plastic zone, total
Delamination Toughening
E
TD C(T) specimen
TRIP Toughening
F
Crack propagation
Fracture surface
Pre-crack
Pre-crack tip
Notch tip
Crack tip
Fracture surface
Short delamination cracks
Mid-plane section
Through-thickness section
H
Crack propagation
Crack tip
6 µm
Crack tip
G
Through-thickness section
Delamination cracks
Short cracks
PAGBs
Crack tip
Plastic zone, TRIP
Plastic zone, total

Fig. 3. Toughening mechanisms in the steel. (**A** and **E**) The schematic diagrams of the RD and TD C(T) specimens showing the various sections for microstructure characterizations. (**B** and **F**) The fracture surfaces of the RD and TD C(T) specimens, clearly showing the thin-layer delamination bands on the fracture surface. (**C** and **G**) The SEM images captured on the through-thickness section normal to the fracture surface show the development of delamination cracks along PAGBs. Short delamination cracks (blue arrows) and deeply penetrated ones (red arrows) are found in the RD specimen whereas only shallow-penetrated delamination cracks formed in the TD specimen. Slender cracks disconnected from the fracture surface (pink arrows) were usually observed in the vicinity of the long delamination cracks. Corresponding schematic diagrams reveal that the significantly elongated PAGBs in the RD specimen facilitate the propagation of delamination cracks, while the short PAGBs and numerous PAGBs perpendicular to the crack propagation in the TD specimen hinder the extension of delamination cracks. (**D** and **H**) EBSD phase maps overlaid with the image quality maps scanned in the vicinity of the main crack tip on the mid-plane section of C(T) specimens. Schematic diagrams delineating the TRIP-toughening mechanism are shown below. The TRIP-induced martensite (α'_{TRIP}) can be distinguished from the martensite matrix (α'_{matrix}) by higher image quality, due to the fact that the α'_{TRIP} grains transformed from the retained austenite have a lower dislocation density (regions bounded by dashed white lines).

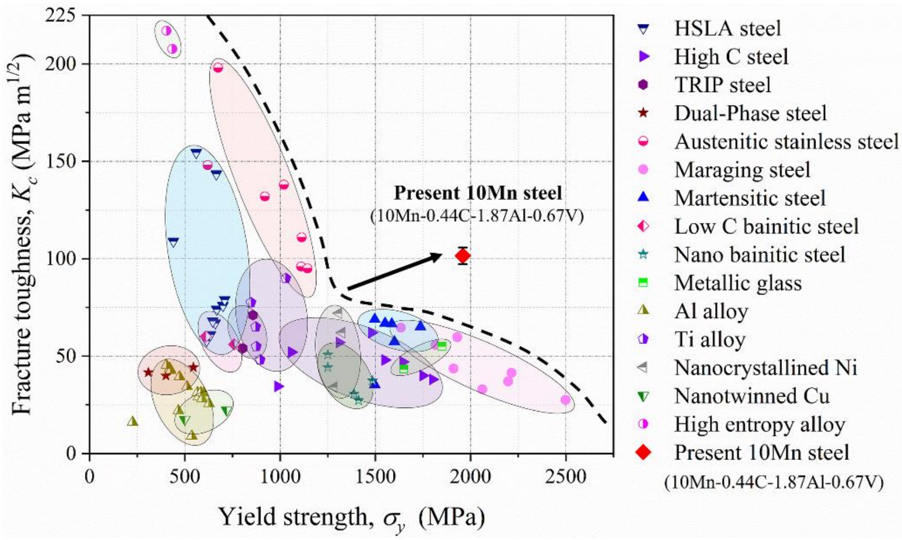

Fig. 4. Ashby map in terms of the fracture toughness versus the yield strength. Our ultrastrong steel overcomes the strength-toughness trade-off shown in most existing structural materials, especially high strength low alloy (HSLA) steels (*29*, *30*), high carbon (C) steels (*31*), TRIP steels (*32*), dual-phase steels (*33*), austenitic stainless steels (*34*, *35*), maraging steels (*18*, *19*, *36*), martensitic steels (*37*, *38*), low C bainitic steels (*39*), nano bainitic steels (*40*), metallic glass (*41*), Al alloys (*42*), Ti alloys (*43*), nanocrystalline Ni (*44*), nanotwinned Cu (*45*), and high-entropy alloys (*6*, *7*). Detailed composition and properties of these compared materials can be found in table S2.